ADVANCED FUNCTIONAL MATERIALS
www.afm-journal.de

Print-and-Plate Architected Electrodes for Electrochemical Transformations Under Flow

*Dylan M. Barber, Sofía Edgar, Michael S. Emanuel, Michael D. Nelwood, Bok Yeop Ahn, Benito Román-Manso, Thomas Cochard, Justin Platero, Kiana Amini, Chris H. Rycroft, Shmuel Rubinstein, Michael J. Aziz, and Jennifer A. Lewis**

Flow cell electrodes are typically composed of porous carbon materials, such as papers, felts, and cloths. However, their random architecture hinders the fundamental characterization of electrode structure-performance relationships during in situ operation of porous electrochemical flow systems. This work describes a "print-and-plate" method that combines direct ink writing of micro-periodic lattices with a two-step metal plating process that converts them into highly conductive (sheet resistance 40 mΩ sq^{-1}) electrodes. Their *operando* performance is assessed in an anthraquinone disulfonic acid half-cell using widefield electrochemical fluorescence microscopy, where output current and fluorescence intensity are in excellent agreement. The pressure drop associated with flow through three electrode designs is determined via simulations from which the most efficient design is identified and manufactured via print-and-plate. Confocal fluorescence microscopy is then used to create a 3D map of the state of charge (SOC) inside this print-and-plate electrode. The experimental state of the charge map is in good agreement with computational predictions. The rapid design, simulation, and fabrication of print-and-plate electrodes enable fundamental investigations of how architected porosity affects electrochemical performance under flow.

1. Introduction

Porous electrodes combine hydraulic permeability with high electron conductivity to electrochemically transform flowing liquid electrolytes. They are widely used in redox flow batteries,[1] fuel cells,[2] electrolyzers,[3] electrosynthesizers,[4,5] and desalination systems.[6,7] The fundamental interplay between advective and diffusive mass transport, electrochemical charge transfer, and ionic and electronic conduction is inherent to electrochemical flow cells. While electrode architecture often varies between applications, understanding and optimizing electrolyte flow through porous electrodes are unifying goals.[1] Of specific interest is the minimization of losses that arise by: pumping electrolyte through porous media, electrical resistance within the electrode, and charge transfer resistance between electrolyte and electrode.[8–12] Minimizing these distinct loss mechanisms

D. M. Barber, S. Edgar, M. S. Emanuel, M. D. Nelwood, B. Y. Ahn, B. Román-Manso, T. Cochard, J. Platero, K. Amini, C. H. Rycroft, M. J. Aziz, J. A. Lewis
John A. Paulson School of Engineering and Applied Sciences
Harvard University
Cambridge, MA 02138, USA
E-mail: jalewis@seas.harvard.edu

D. M. Barber, M. D. Nelwood, B. Y. Ahn, B. Román-Manso, J. Platero, J. A. Lewis
Wyss Institute for Biologically Inspired Engineering
Harvard University
Boston, MA 02215, USA

The ORCID identification number(s) for the author(s) of this article can be found under https://doi.org/10.1002/adfm.202419748

DOI: 10.1002/adfm.202419748

J. Platero
Nanoelectrochemical Analysis and Energy Storage Laboratory (NEST LAB)
Department of Chemistry
School of Science
Navajo Technical University
Crownpoint, NM 87313, USA

K. Amini
Department of Materials Engineering
The University of British Columbia
Vancouver, BC V6T 1Z4, Canada

C. H. Rycroft
Department of Mathematics
University of Wisconsin–Madison
Madison, WI 53706, USA

C. H. Rycroft
Mathematics Group
Lawrence Berkeley National Laboratory
Berkeley, CA 94720, USA

S. Rubinstein
The Racah Institute of Physics
The Hebrew University of Jerusalem
Jerusalem 9190401, Israel

typically requires design trade-offs between hydraulic permeability, electrode conductance, and specific surface area.

Unfortunately, the most ubiquitous porous electrodes, e.g., carbon felts,[10,13–16] papers,[10,17–22] and cloths,[10,17,18,23–26] exhibit poorly controlled composition and geometry. For example, electrospun carbon papers consist of random fibrous mats resulting in 3D motifs that differ microscopically from electrode to electrode. By contrast, architected electrodes composed of 3D periodic lattices offer a promising avenue for elucidating structure-property-performance relationships. Such electrodes enable the direct translation of computational designs into 3D printable electrodes, including lithium-ion micro-batteries,[27] and candidate designs in which the removal of certain features may actually increase voltage efficiency at a given current density.[28] Despite the power of additive manufacturing, most printable inks and photocurable resins are poorly conductive. Efforts to enhance their conductivity have focused largely on incorporating a percolated network of metallic nanoparticles within polymer matrices to achieve electrical resistivities of $\approx 10^{-5}$ Ω cm.[29] Alternately, van der Heijden et al. and Beck et al. used stereolithography and direct ink writing, respectively, followed by pyrolysis to generate conductive carbon electrodes.[30,31] While electroless metal plating[32,33] has been reported previously,[34–36] it has not been used for 3D-printed porous electrodes.

Here, we report an integrated design, modeling, and 3D print-and-plate method for fabricating architected electrodes composed of micro-periodic lattices (filaments ≈20 µm diameter) that are coated conformally via gold plating to yield a sheet resistance of 40 mΩ sq^{-1}. We use these architected electrodes in 4D visualization experiments combining chronopotentiometry with widefield electrochemical fluorescence microscopy. These experiments simultaneously visualize and quantify *operando* electrochemistry, including electrochemical conversion, advection, and diffusion.[37] Next, we numerically solve the governing equations for three electrode architectures by strategically removing printed filaments (lattice struts) to alter the flow path and corresponding pressure drop. The optimal design (lowest pressure drop) is then fabricated and used as an architected electrode in an anthraquinone 2,7-disulfonic acid (AQDS) half-cell, where reduction affords fluorescent H_2AQDS. Confocal electrochemical fluorescence microscopy is used to directly visualize electrochemistry through the electrode thickness. Finally, confocal fluorescence data is converted to a 3D state of charge (SOC) map, revealing that conversion is highest at the electrode-electrolyte interface and that the mean SOC is 0.19 across the imaged volume, in good agreement with a simulated analog (SOC = 0.22). Together, these results show that print-and-plate electrodes can be rapidly designed, modeled, and fabricated with controlled architecture to enable through-volume, *operando* quantification of electrochemistry.

2. Print-and-Plate Electrode Fabrication

Direct ink writing, an extrusion-based 3D printing method, is used to pattern a graphene nanocomposite (GNC) ink, which is readily extruded through a 30 µm nozzle. The ink is composed of a commercially available thermoplastic polyurethane (TPU), graphene nanoplatelets (GNP), and dimethylformamide (DMF), which inhibits physical crosslinking of the TPU prior to printing (**Figure 1a**). While this ink exhibits shear thinning behavior (Figure 1b), its storage (G') and loss (G'') moduli are nearly identical at low shear stresses (Figure 1c).[38,39] However once the ink exits the nozzle, the solvent (DMF) evaporates, leading to a pronounced solidification that allows the printed filaments to span gaps as large as 700 µm (>20x larger than the filament diameter), with negligible sagging (Movie S1, Supporting Information). Solvent-driven changes in ink elasticity are particularly well suited to printed lattices composed of microscale filaments with a high surface-to-volume ratio. The printed lattices are composed of a rectangular region with overall dimensions 6 mm x 3 mm and two long tails that facilitate handling during subsequent processing steps. These architected electrodes are composed of printed filaments with a diameter ≈20 µm arranged in seven-layer woodpile structure with a total thickness of ≈140 µm (Figure 1d; Movie S2, Supporting Information). SEM images of a 3×3 unit cell (100 µm x 100 µm) within these printed lattices (Figure 1e) and of individual filaments (Figure 1f) highlight their periodic nature and surface roughness, respectively.

Each printed lattice is subjected to a two-step plating process to enhance its electrical conductivity (**Figure 2a**). First, they (Figure 2a, left) are plated in nickel (Figure 2a, center) by submerging each lattice in a commercial electroless Ni plating solution at 70 °C. Next, they are electroplated with a thin layer of gold (Figure 2a, right) to further enhance conductivity and render their surfaces electrochemically inert. The resulting print-and-plate electrodes (Figure 2b) exhibit excellent fidelity to the original printed lattices (Figure 1d), yet contain a conformal gold coating across the entire surface of each strut. SEM images, taken in the xy plane, show a square region of 3 × 3 unit cells (Figure 2c) with a uniform metal coating across the printed struts (Figure 1e). Higher resolution imaging (Figure 2d), reveals that the plated surface is rough, consistent with that of the underlying printed filament (Figure 1f), and is composed of rounded grains.

To further characterize these architected electrodes, we cryo-fractured the as-printed and dried (Figure 2e), Ni-plated (Figure 2f), and bilayer Ni-Au-plated (Figure 2g) configurations at each stage of the fabrication process and directly imaged them in the yz plane. We find that the filament cross-section of the as-printed lattices deviates slightly from the desired circular shape with a mean diameter of ≈19 µm along the z-axis and ≈21 µm along the y-axis. Note: the effective filament diameter is considerably smaller than that of the printing nozzle (30 µm inner diameter) due to slight under-extrusion of the GNC ink during printing followed by solvent evaporation. As expected, the filament diameter increased to values of ≈23 µm and 26 µm after nickel plating and to final values of ≈24 µm and 29 µm after gold plating, along the z- and y-axes, respectively. Concomitantly, the vertical gap between alternating layers decreased from 14 µm (as-printed) to 10 µm (Ni-plated), then 8 µm (bilayer-plated). Figure 2h reveals their distinct multicore-shell filamentary architecture composed of an organic GNP/TPU core coated first by nickel (≈2.3 µm thick) and then gold (≈630 nm thick). Finally, we measured the sheet resistance of these architected electrodes at specified intervals during the plating process (Figure 2i). The sheet resistance of the as-printed electrodes exceeded our measurement capabilities. However, the sheet resistance R_s progressively decreased to 780 mΩ sq^{-1} after Ni plating for 10 min, then to 40 mΩ sq^{-1} after 20 min of Ni plating followed by 20 min of gold electroplating.

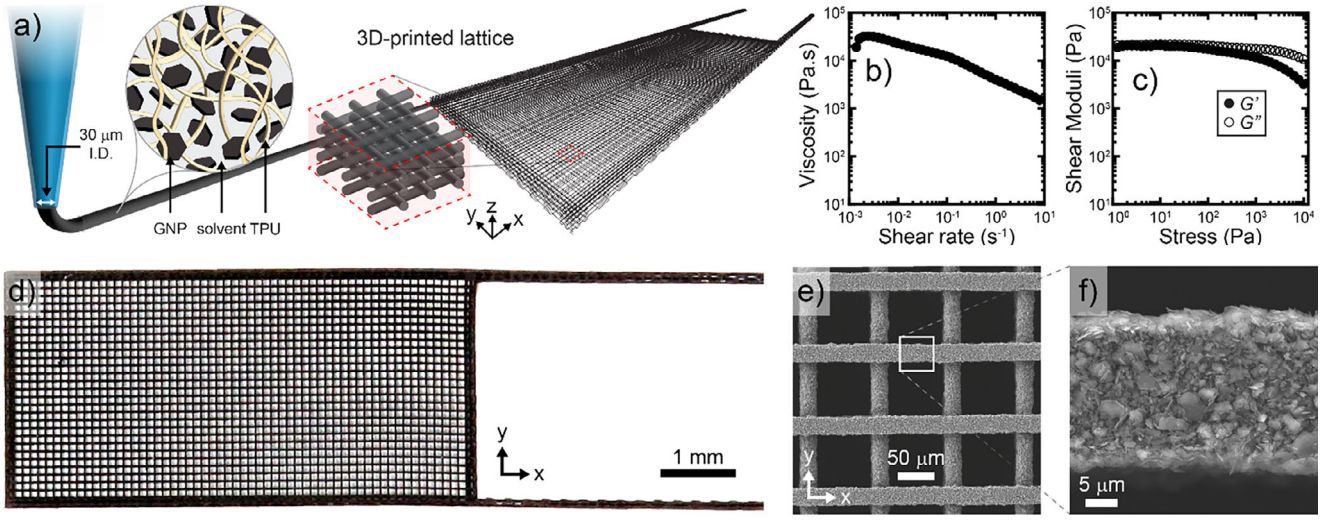

Figure 1. Ink formulation, printability, and microstructure. a) Direct ink writing of a graphene nanocomposite (GNC) ink, composed of graphene nanoplatelets (GNP), thermoplastic polyurethane (TPU), and dimethylformamide solvent, through a glass nozzle with a 30 µm inner diameter to afford an architected lattice. The GNC ink exhibits, b) shear-thinning behavior for shear rates 10^{-3}-10^{1} s^{-1}, and c) quasi yield-stress behavior for shear stresses 10^{0}–10^{4} Pa at 1 Hz oscillation frequency. d) Photograph of a representative lattice with 100 µm x 100 µm unit cells in the xy plane; e,f) scanning electron micrographs reveal uniform filament dimensions (e) and a GNP-derived rough surface microstructure in the extruded filament (f).

3. Electrochemical Fluorescence Microscopy in Print-and-Plate Electrodes

As an initial demonstration, we evaluated architected electrodes composed of a woodpile structure (Figure 2) via widefield electrochemical fluorescence microscopy in which AQDS is used as a catholyte fluorophore.[37,40,41] For this experiment, the AQDS half-cell is prepared with the print-and-plate electrode positioned against a flow field prepared by patterning an array of channels and ribs in PDMS to manipulate the velocity field, and placed on a 3D printed base embedded with a glass cover slide to enable direct visualization via a microscope (**Figure** 3a, top). The two-electron reduction of AQDS in an acidic medium yields fluorescent H_2AQDS (Figure 3a, bottom); this redox-activated fluorescence is used to map the evolving H_2AQDS concentration field in real time. The fluorescence in the AQDS half-cell is monitored while applying periodic pulses of reductive overpotential at 50, 100, 150, and 175 mV amplitude (Figure 3b, top and Figure 3d) versus open-circuit voltage (OCV) to the print-and-plate electrode. During the experiment, AQDS solution is pumped at 5 mL h^{-1}, leading to an average velocity of 3.8 mm s^{-1}, and pulses are sustained for 30 s, separated by 10 s intervals at OCV. Both current (*i*, Figure 3b, center) and absolute pixel-by-pixel fluorescence intensity (*I*) outputs are recorded as a function of time and applied potential.

Output current increases with overpotential. However, each stepwise transition gives rise to a transient (≈0.5–1.0 s) current spike before decaying to an equilibrium value. Moreover, this occurs for both increases and decreases in applied voltage, but with opposite polarity in each case. We estimate an RC timescale of ≈2 ms for our electrode in aqueous acid, eliminating capacitance as a contributor to this effect. We note that 10 s intervals at OCV offer sufficient time for the transport of reduced species away from the electrode surface and the replenishment of unreacted AQDS. Upon repolarization, local regions close to the electrode match the bulk AQDS concentration, leading to transient low resistance until AQDS is again locally depleted and the system returns to a steady-state. Upon depolarization, the current spike is negative, suggesting a reversed current due to an initially high, transient local concentration of reduced species.

Fluorescence data are similarly acquired and analyzed for these print-and-plate electrodes. Initially, we collected a background image at OCV, which is then subtracted from the raw time series. This process is shown schematically in Figure 3c, with a representative frame at OCV (Figure 3c, left), another with an applied potential (Figure 3c, center), and a third representing the expected spatial distribution of $I - I_{OCV}$ (Figure 3c, right). The corresponding data are collected in a 26 × 26 unit cell domain (Movie S3, Supporting Information); a 4 × 4 unit cell inset (Figure 3d; Movie S4, Supporting Information) highlights behavior at the length scale of individual filaments and the gaps between them. The mean frame-by-frame gray value is plotted in Figure S1 (Supporting Information), bottom (full 26 × 26 unit cell domain) and Figure 3b, bottom (4 × 4 unit cell inset), showing excellent fidelity between input overpotential *E*, output current *i*, and mean fluorescence intensity $I - I_{OCV}$, across both length scales.

Figure 3d shows the OCV micrograph (left) subtracted from the remaining data in the 4 × 4 unit cell domain, i.e., $I - I_{OCV}$, including the micrographs taken at E = 50, 100, 150, and 175 mV. For the OCV micrograph, we observe weak fluorescence in the apertures between filaments. We attribute this to the starting AQDS, which emits faintly above λ_{em} = 530 nm upon excitation by λ_{ex} = 405 nm.[42] The use of a widefield objective imparts a depth of field of ≈780 µm, roughly fivefold larger than the electrode thickness. Hence, the fluorescence of Figure 3d captures light from the entire electrode rather than a localized plane of fixed z value.

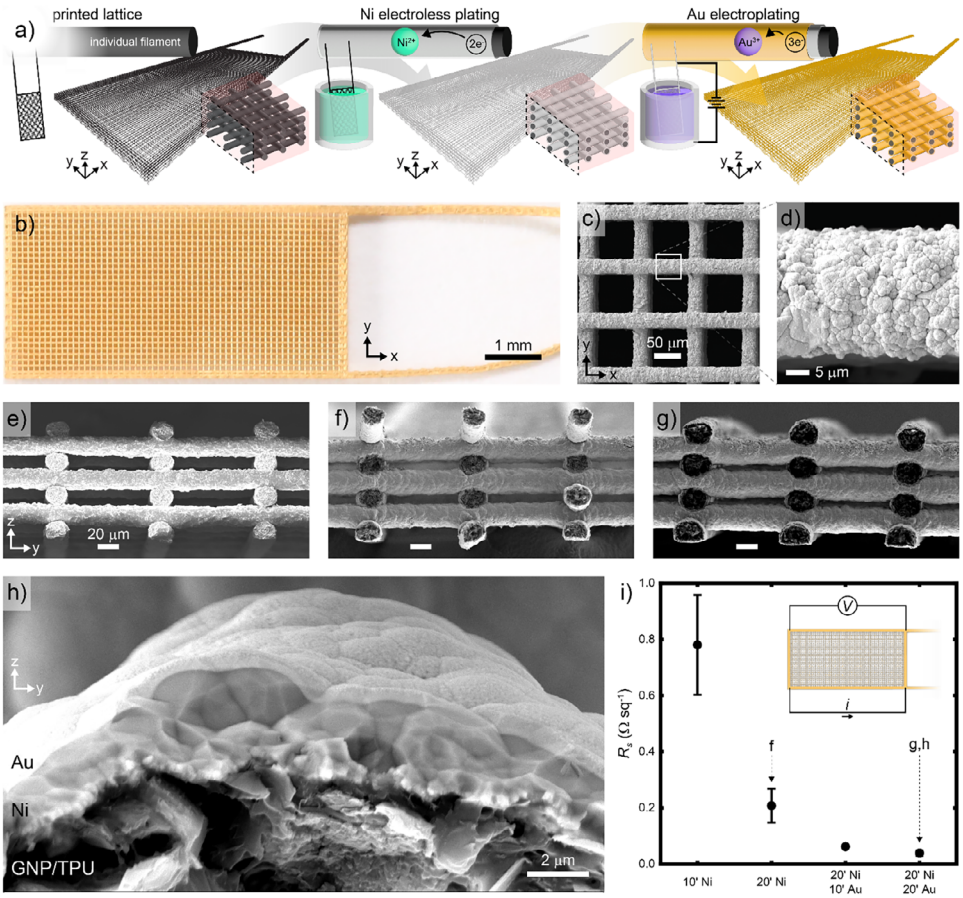

Figure 2. Metal plating of printed lattices. a) schematic of the metal plating pathway: the printed lattice (left) is subjected to electroless plating to afford the Ni-coated lattice (center), then electroplated to afford the final gold-plated lattice (right); b) photograph of a representative lattice with symmetric 100 µm x 100 µm unit cells in the xy plane after 20 min each of Ni and Au plating; SEM micrographs in the xy plane reveal uniform filament plating (c) and rough surface microstructure (d); e–h) SEM micrographs of cryo-fractured lattices in the yz-plane after printing (e), 20 min Ni plating (f), then 20 min Au plating at low (g) and high (h) resolution. i) sheet resistance R_s (Van der Pauw method) of plated lattices with successively increasing metal plate duration; inset schematic shows measurement approach, with applied current i and measured potential V. Data are represented as mean ± 2 standard deviations, $n = 3$.

After subtracting the background, we observe both qualitatively (Figure 3d; Movies S3–S4, Supporting Information) and quantitatively (Figure 3b; Figure S1, Supporting Information) that the fluorescence output correlates positively with applied overpotential and output current. During periods of applied overpotential, the greatest fluorescence intensity emerged at the surface of the printed filaments, rather than in the pores between. Finally, Figures S2 and S3 (Supporting Information) reveal the excellent agreement between OCV-subtracted mean fluorescence intensity and mean steady-state current at both the mesoscopic (26 × 26 unit cells, Figure S2, Supporting Information) and microscopic (4 × 4 unit cells, Figure S3, Supporting Information) length scales. These observations support our hypothesis that fluorescence data can be used to extract quantitative information about steady-state electrochemical conversion. Moreover, both current and mean gray values exhibit a relatively small increase from 150 to 175 mV. We posit that the current, which increases from $i = 0.84 \pm 0.05$ mA at $V = 150$ mV to $i = 0.88 \pm 0.07$ mA at $V = 175$ mV) suggests an increase in internal resistance that is consistent with the onset of mass transport limitation.

4. Electrode Design Informed by Simulations

Prior studies of simulated flow cells suggest that strategic removal of electrode mass can lead to more effective advection of reacted material from the electrode surface, thereby improving voltage efficiency.[28] To investigate this for print-and-plate electrodes, we simulate three new electrode architectures (**Figure** 4a–f) designed to decrease flow resistance during pressure-driven flow in the positive x direction. The first of these, termed "stagger," (Figure 4a) employs an offset between y-oriented filaments (perpendicular to the flow path) in layers two, four, and six to obviate local pinch-points that might increase the hydrodynamic resistance of the electrode. Filaments in layers two, four, and six employ a 200 µm step size, affording a twofold decrease in filament density in these layers compared to the initial square lattice design (100 µm step size) of Figures 1–3. The second strategy, termed "stack," (Figure 4b) separates transverse filaments by stacking double layers of x-oriented filaments between them. In this case, the transverse filaments are moved from layers two, four, and six (seen in both the square lattice of Figures 1–3 and the

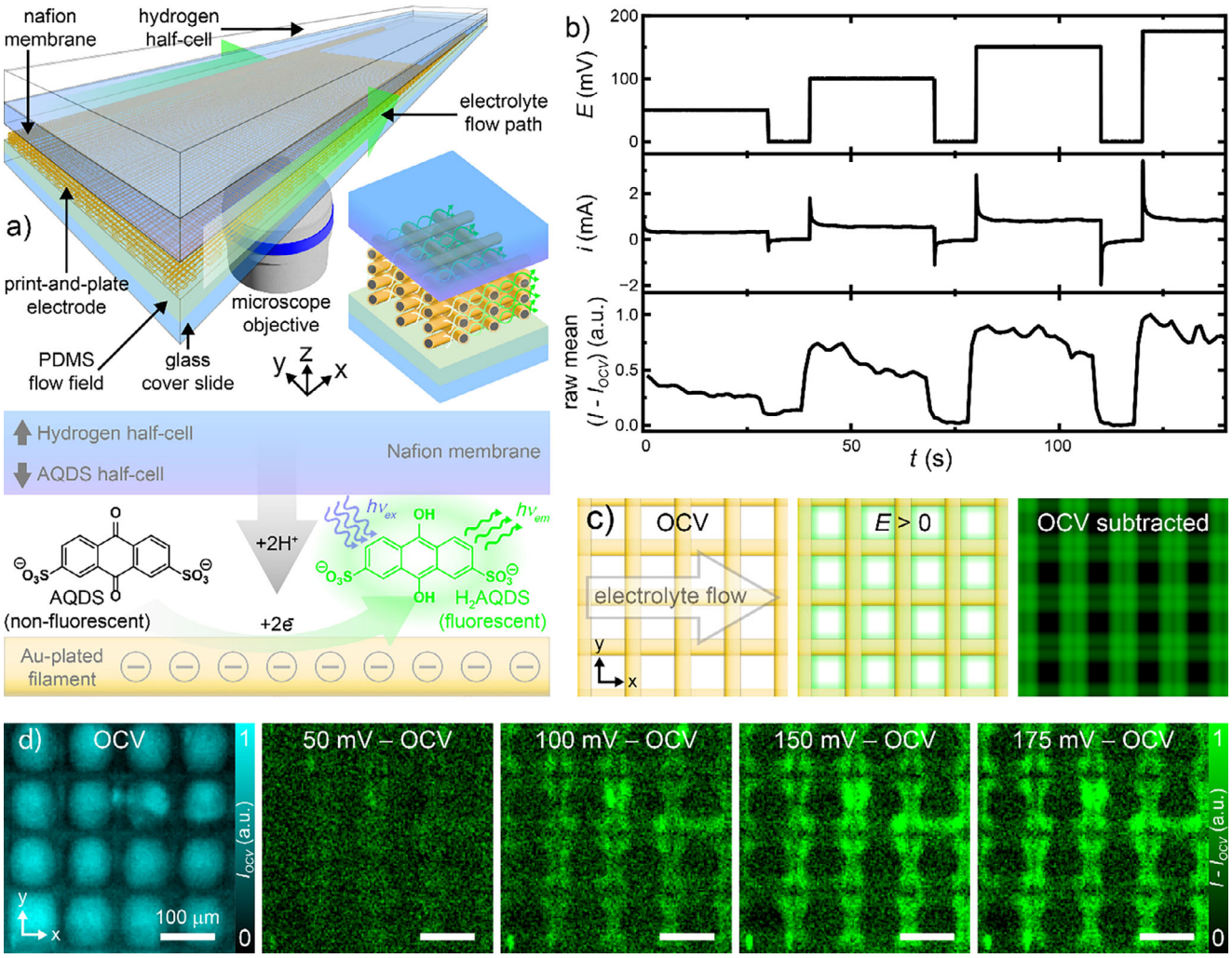

Figure 3. Electrochemical fluorescence microscopy in print-and-plate lattices. a) schematic of the electrochemical fluorescence cell, including an opposed hydrogen half-cell, a nafion membrane, and a print-and-plate electrode with a flowing electrolyte solution, separated from a microscope objective by a PDMS flow field on a glass cover slide; the inset (right) shows a 2 × 2 unit cell electrode domain between the nafion membrane (top) and flow field on a cover slide, with electrolyte flowing between filaments; the reaction scheme (bottom) shows the two-electron reduction of AQDS to H_2AQDS in an acidic medium, activating its fluorescence. b) Reducing overpotential (top), measured current (center), and mean OCV-subtracted gray value (bottom) as a function of time in a stepwise chronopotentiometric fluorescence experiment; c) schematic illustrating our data processing pathway, consisting of an OCV background image (left) subtracted from a micrograph with applied potential (center) to afford a current-derived fluorescence image (right). d) The selected OCV background frame (left) and representative background-subtracted micrographs at 50, 100, 150, and 175 mV applied overpotential.

stagger lattice of Figure 4a) to layers one, four, and seven, expanding the flow aperture between consecutive transverse filaments. The third, termed "stagger-stack" (Figure 4c) combines the offsetting strategy of the stagger lattice with the increased vertical separation of the stack lattice.

Flow simulations are carried out using an embedded boundary method based on the incflo library[43] for incompressible flow problems. The incflo library in turn relies on AMReX for adaptive meshing.[44] A uniform pressure is imposed at the inlet that is iteratively set to achieve a flow rate of 10.0 mL hr^{-1}, leading to an average velocity of 7.6 mm s^{-1}. The simulation is based on a coarse grid with 5.0 µm resolution and two levels of mesh refinement to resolve solid–liquid boundaries to a 1.25 µm resolution, leading to geometries with 780 to 840 million cells. The 3D xy and xz projections of simulated local fluid speed are shown in the heat maps of Figure 4d (stagger), 4e (stack), and 4f (stagger-stack). The model predicts a broad range of hydraulic resistance across these three lattice designs with respective pressures of 244, 419, and 136 Pa required to achieve the specified flow rate. Pumping losses are minimized in the stagger-stack geometry, while the largest pressure drop occurs in the stack geometry. The lower panel of Figure 4e shows small, bright red pinch points where the entire flow must squeeze through a small cross-section at high speed, leading to high required pressures and concomitant viscous losses. The analogous panel of Figure 4f shows a significantly wider aperture at the narrowest point, hence a lower hydraulic resistance.

The simulated stagger-stack design is realized by the print-and-plate electrode shown in Figure 4g–i (printed in Movie S5, Supporting Information). Figure 4g shows a 3.5 × 3.5 unit cell

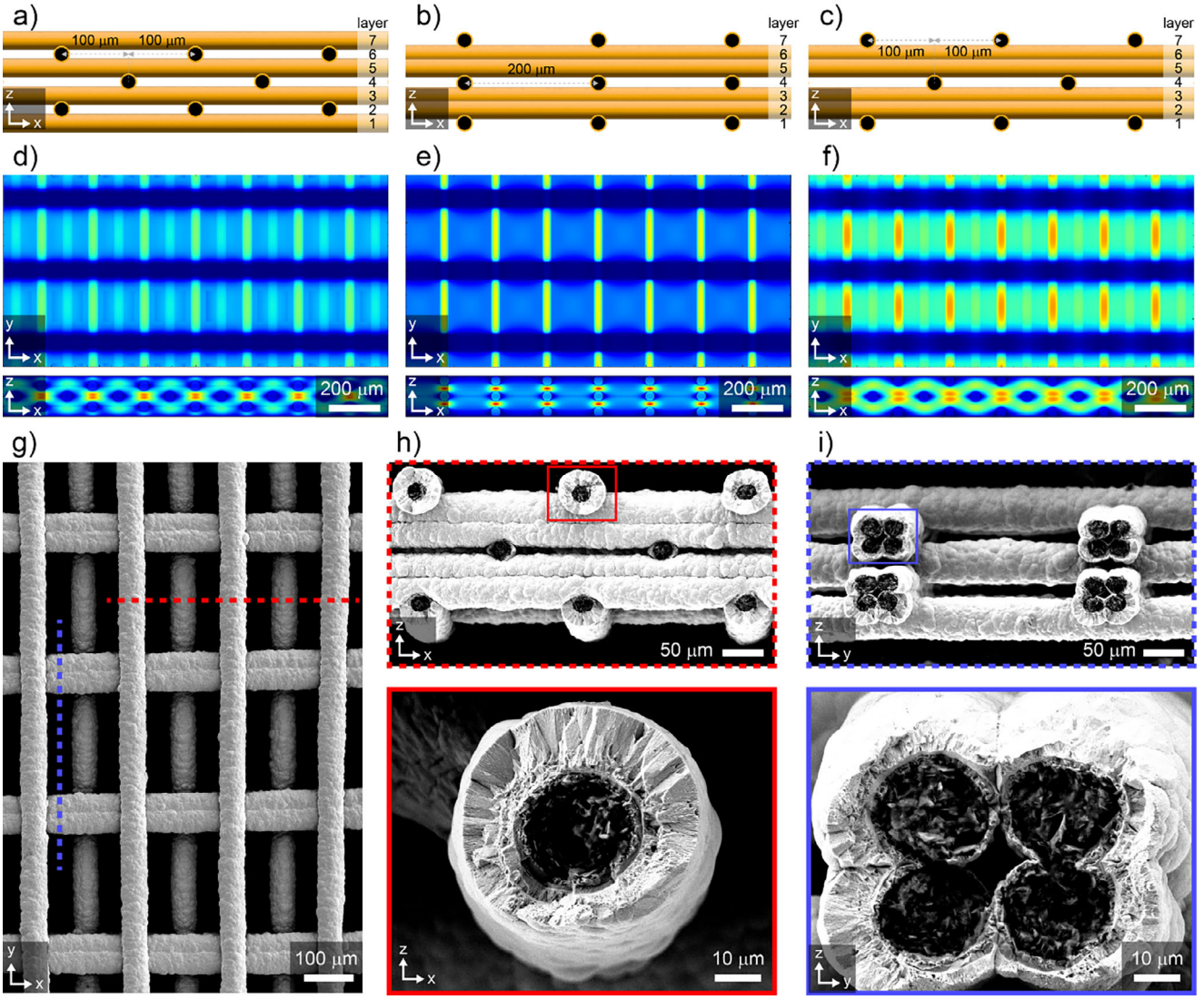

Figure 4. Print-and-plate electrode architecture guided by computational design. Schematics (xz plane) of proposed stagger a), stack b), and stagger-stack c) lattice architectures; projected electrolyte velocity maps in the yz (top) and xz (bottom) planes for stagger d), stack e), and stagger-stack f) structures; g) a scanning electron micrograph of a print-and-plate stagger-stack lattice in the xy plane; the horizontal dashed line corresponds to cryo-fractured cross-sections (h), which reveal the target stagger-stack structure at low magnification (top) and a single plated filament at high magnification (bottom); the vertical dashed line of (g) corresponds to cryo-fractured cross-sections (i), which reveal the supporting bilayer structure of "stacked" layers two, three, five, and six at low (top) and high (bottom) magnification.

domain in the xy plane. Consistent with the schematic of Figure 4c, layer one (nearest the camera) is composed of y-oriented filaments spaced at 200 µm intervals. Above this is a double layer of x-oriented filaments (layers two and three), followed by layer four, which is aligned in the y-direction and staggered between the filaments of layer one. The cross-sectional data are collected using lattices cryo-fractured according to the dashed guidelines in Figure 4g. For example, the horizontal dashed line corresponds to the xz cross-section of Figure 4h, which is in excellent agreement with schematic Figure 4c, showing staggered layers one, four, and seven oriented in the y-direction, with double-layers 2+3 and 5+6 oriented parallel to x. The vertical dashed line of Figure 4g corresponds to the yz cross-section (Figure 4i) and shows the cross-sections of the fourfold square bundles oriented along the x-direction. These possess a characteristic clover-leaf profile that originates from the initial print geometry and is propagated during metal plating, affording grooves of ≈5–10 µm depth on each face. Together, these micrographs indicate good agreement with the simulated stagger-stack lattice.

5. 3D State-of-Charge Mapping in Print-and-Plate Electrodes

After optimizing, printing, and plating the simulated electrode design, we characterized its *operando* behavior using electrochemical confocal fluorescence microscopy (**Figure 5**). In this experiment, fluorescence in a small region (772 µm x 772 µm) of the print-and-plate stagger-stack electrode is visualized at a fixed

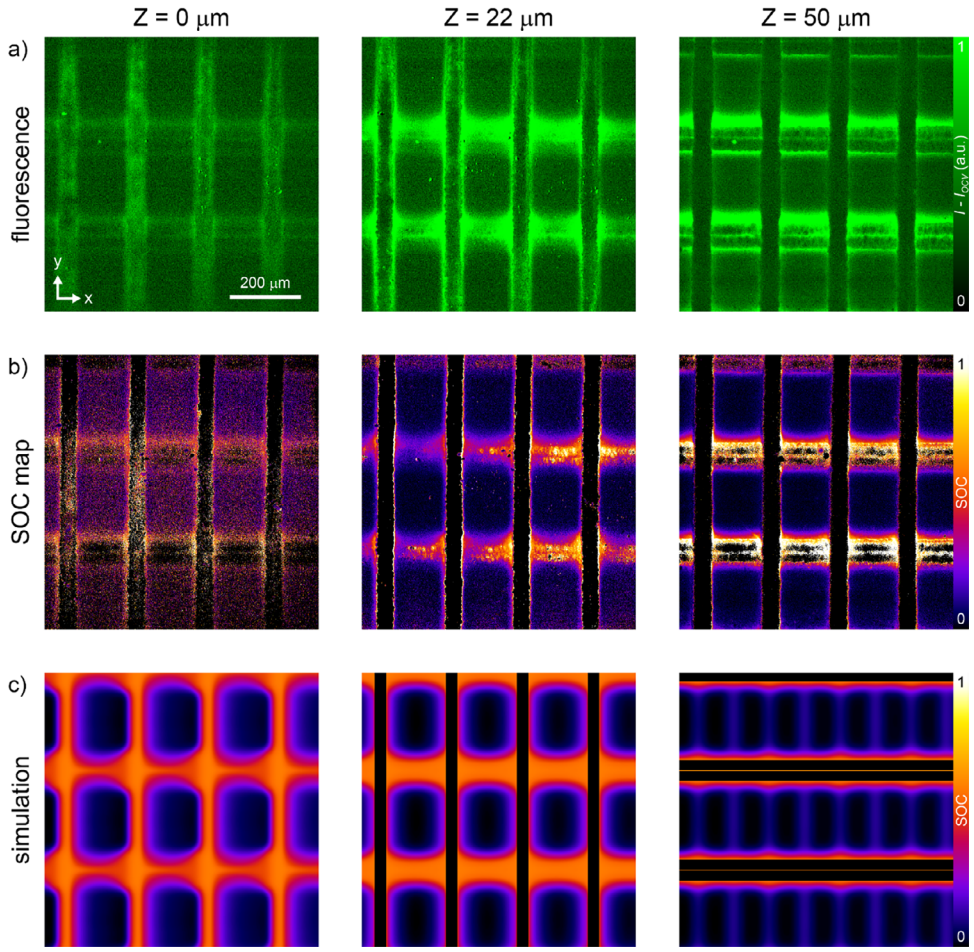

Figure 5. 3D quantitative state-of-charge mapping. a) Background-subtracted confocal electrochemical fluorescence micrographs of a stagger stack print-and-plate electrode at depth z = 0, 22, and 50 μm from the underlying glass coverslip; calibrated experimental b) and simulated c) state of charge maps at the same three positions. The microscope objective is positioned beneath the layer one filaments so that, as the z-stack progresses, layer one, then layer two, etc., filaments are successively in focus.

location in the xy plane and variable depth, z. While fluorescence can be confocally resolved in three dimensions, it is only possible to do so along unobstructed sightlines. Unlike the woodpile lattice, the stagger-stack architecture is particularly useful for depth-dependent visualization (Figures 1–3; Movies S1–S4, Supporting Information) because its midplane layer four is optically accessible to the microscope, whereas layers one and two in conventional woodpile electrodes obstruct all deeper layers. Figure 5a shows selected, OCV-subtracted fluorescence of z-slices at depths 0, 22, and 50 μm from the PDMS flow field beneath the electrode, revealing bright fluorescence at the print-and-plate filament surfaces. This data corresponds to Movie S6 (Supporting Information), where individual frames represent 2 μm intervals to a depth of 130 μm (details in Supporting Information).

A key objective of this work is quantitative 3D mapping of the state of charge (SOC), a unitless term that quantifies conversion of the electrolyte in the electrochemical cell according to SOC = $[H_2AQDS]/([AQDS] + [H_2AQDS])$. To achieve this, a reference z-stack is collected using a 10 mM solution of pure H_2AQDS flowing at a volumetric flow rate of 2 mL h^{-1}, matching the operating conditions of the running electrode shown in Figure 5a. The voxel size is 0.75 μm x 0.75 μm x 2.0 μm, defined by the xy pixel dimensions for each slice and the size of each z step. Subtracting the OCV data set from our reference stack afforded a fluorescence map for SOC = 1, which we used to calibrate our experimental data. Dividing the data of Figure 5a by this calibration map yields the desired 3D SOC map, while a mask excludes voxels in filament cores.

Additionally, SOC is simulated for the stagger-stack electrode design under identical conditions based on advection, diffusion, and electrochemical reactions with Butler-Volmer kinetics. The incompressible flow is held constant using the same grid with 1.25 μm resolution and run to steady-state. A detailed description of the image processing pathway and simulation method is contained in Methods.

Figure 5b,c shows the experimental and simulated SOC maps corresponding to the frames of Figure 5a, whereas Movies S7 and S8 (Supporting Information) reveal the entire experimental and simulated data sets, respectively, to a depth of 130 μm. At z = 0 μm (Figure 5b, left), we observe a small but nonzero SOC distribution in the electrolyte-filled gaps between filaments, and higher SOC at the filament and bundle edges. The diffuse nature of the

SOC map at this depth may be an artifact of scattering by the liquid-PDMS interface, but the larger SOC around the filaments is consistent with the simulated SOC map (Figure 5c, left). Importantly, at z = 22 µm (Figure 5b,c, center), the experimental and simulated SOC maps are in excellent agreement. For example, SOC in the spaces between filaments is negligible, the edges of layer one filaments are consistent with high local SOC, and the bottom surface of x-oriented layer two shows relatively high SOC. Both the edges of the layer one filaments and the bottom of layer two filaments resolve the roughness of the metal-plated surfaces, with feature sizes (≈10 µm) and texture (round nodules) consistent with the SEM data of Figures 2 and 4; this is especially striking in the case of the layer two filaments because these features are not well resolved in the fluorescence map of Figure 5a, center, yet are well-defined in the SOC map of Figure 5b, center. This resolution of fine features includes the groove at the bottom of layer two. We also note relatively high SOC at the junction points between x- and y-oriented filaments, again in excellent agreement with the simulation. Finally, at z = 50 µm (Figure 5b,c, right), the inter-filament spaces maintain a relatively low SOC, while the edges and central groove of x-oriented layer 2+3 bundles show locally high SOC. At this depth, the experimental frames exhibit the shadows from the layer one filaments: although these filaments lie outside of the focal plane, they block light from greater depths within the lattice. In addition, the experimentally derived SOC in the periphery of the x-oriented bundles is slightly larger than the simulation. Nevertheless, these data also reflect qualitative agreement between experiment and simulation. In addition to individual, frame-by-frame SOC maps, aggregate experimental and simulated SOC combining all 66 frames of data are in good agreement, with global average SOC = 0.19 (experiment) and 0.22 (simulation), offering mutual validation to both approaches.

In summary, we have integrated electrode design and simulation with a fabrication approach, termed print-and-plate, for creating architected electrodes that enable through-thickness electrochemical fluorescence imaging. By tracking the transient dynamics of the output current with stepwise changes in overpotential, we demonstrated excellent agreement between the output current and fluorescence intensity along with the onset of mass-transport limitation at overpotentials with a magnitude exceeding ≈150 mV. Using computational modeling, we assessed three candidate electrode designs and used this output to guide their print-and-plate construction. We then mapped their 3D fluorescence and state of charge in an active electrochemical cell. This integrated approach would be difficult to achieve in conventional carbon paper or felt electrodes due to their random, irreproducible configurations. This platform offers a new avenue for fundamental studies of complex electrode designs and electrochemical phenomena for a broad range of applications.

6. Experimental Section

Materials: Anthraquinone 2,7-disulfonic acid (AQDS, ≥80%, AFG Scientific), ACS Reagent Sulfuric acid (H_2SO_4, 1 M (diluted from 18 M with deionized water), 95.0–98.0%, Sigma), Vanadium(IV) oxide sulfate hydrate ($VOSO_4 \bullet xH_2O$, 97%, Sigma–Aldrich),Vanadium Oxide (V_2O_5, ≥98%,Sigma–Aldrich), Elastollan Soft 35A 12P000 thermoplastic polyurethane (TPU, BASF), dimethylformamide (DMF, 99.8%, anhydrous), 1-methylpyrrolidinone (NMP, 99.5%, anhydrous), graphene nanoplatelets (GNP, C-300 grade), poly(sodium 4-styrene sulfonate) (PSS, average M_W 70 kDa), poly(ethylene imine), (PEI, average M_n = 1.8 kDa by GPC, average M_W = 2 kDa by LS, 50 wt.% in H_2O), tin(II) chloride ($SnCl_2$, reagent grade, 98%), palladium(II) chloride ($PdCl_2$, 99%, Reagent-Plus, Sigma–Aldrich), isopropanol (99.0%, ACS Reagent Grade for histology, VWR), hydrochloric acid (HCl, ACS Grade, 36.5–38.0% solution, EMD Millipore Corporation), nickel electroless plating solution (Caswell Inc.), and 24K bright gold plating solution (Gold Plating Services) were used as received without further purification. The hydroquinone (reduced) form of AQDS (H_2AQDS) was prepared for fluorescence calibration experiments by discharging previously charged 50% SOC AQDS (non-capacity limiting side) against a capacity-limiting side of initially fully oxidized AQDS in a flow cell under nitrogen. Coulomb counting was utilized to determine the SOC of the capacity-limiting side and charged it to 100% SOC.

Ink Preparation: 7.5 g of a 20 wt.% solution of TPU in DMF was weighed into a 50 mL polypropylene centrifuge tube, diluted to 15 mL in DMF, and homogenized by shaking. 1 g of GNP was added, and the mixture was homogenized by shaking. The mixture was diluted once more with DMF to a total volume of 30 mL and homogenized again. The mixture was then sonicated for 4 h, then subjected to 3x (centrifuge at 1000 RPM for 2 min, collect supernatant). The resulting viscous black suspension was distributed across 2 50 mL centrifuge tubes and precipitated by adding two volume equivalents of isopropanol, then shaking for 5 min. Phase separation was accelerated by centrifugation at 4000 RPM for 10 min, then the black pellets from both centrifuge tubes were combined in a speed mix cup and placed in a vacuum chamber for 30 min to remove isopropanol. Then, 400 mg DMF and 55 mg NMP were added, and the mixture was mixed in a planetary mixer (SpeedMixer DAC 600.2; FlackTek, Inc.) for a total of 6 min at 2000 RPM. The mixture was subjected to two more cycles (30 min vacuum, 6 min mixing at 2000 RPM) to afford the graphene nanocomposite ink as a tacky, black viscoelastic liquid.

Rheological Measurements: Ink rheological properties were characterized with a Discovery HR20 rheometer equipped with a 20 mm parallel plate stainless-steel geometry and a 500 µm gap. Apparent viscosity η was measured as a function of increasing shear rate from 10^{-3} to 10^{1} s^{-1} at 20 °C. Storage (G') and loss (G'') shear moduli were measured using direct stress control at an oscillation frequency of 1 Hz from 10^{0} to 10^{4} Pa.

Printing: The ink was loaded into 3 cc syringe barrels (Nordson EFD). The ink-filled syringe was then fitted with a silanized pre-pulled glass nozzle with 30 µm inner diameter (World Precision Instruments TIP30TW1LS01), capped, and centrifuged for 20 min at 4500 RPM to remove bubbles. Then, the ink-loaded syringe barrel was placed in a high-pressure dispensing tool (Nordson EFD) and connected to an electronic pressure regulator (Ultimus V, Nordson EFD). The printhead (syringe, high-pressure dispensing tool, nozzle) was mounted on a custom three-axis cartesian motion stage (Aerotech, Inc., Pittsburg, PA, USA). The electronic pressure regulator was controlled via a serial connection (RS-232) to the motion controller (A3200, Aerotech, Inc.). A glass slide (75 mm x 50 mm x 1 mm) was cleaned by rinsing with soap water, deionized water, and acetone. Then, a solution of 2 wt.% PSS in milli-Q water was passed through a syringe filter (PALL Acrodisc 25 mm PTFE syringe filter 1 µm pore size), and spin-cast onto the freshly cleaned glass substrate (20 s at 500 RPM, 10 s at 150 RPM) and mounted on the motion stage beneath the printhead for use as a substrate. The substrate was aligned with the printhead axes to eliminate substrate tilt, and the toolpath and applied pressure were programmed and controlled via manually written G-code.

Plating: Printed lattices included an initial meander to equilibrate ink flow, and several lattices were typically printed in a single batch without stopping. Before release from the substrate, a razor blade was used to sever the printed lattice from the initial meander and subsequent lattice in each print so that each lattice was an independent monolith on the substrate surface. Then, the substrate with adhered lattices was placed in a large weigh boat, and reverse osmosis water was added to the surface to dissolve the underlying PSS layer, releasing the printed latices from the substrate. After release, lattices were transferred to a 20 mL vial filled with milli-Q water, shaken to fully submerge, then subjected to brief (≈2 s) pulses in a sonication bath to release trapped air bubbles. The water was twice decanted and replaced, for a total of 3 × 20 mL washes. The

lattices were placed on a dry Kimwipe and left in a vacuum chamber for 30 min to evaporate the remaining water. Then, 5 mL of Loctite 5 mine Quick Set Epoxy was manually mixed and spread on a new glass slide, and the lattices were adhered by the tip of one tail each. The glue was given 2 h to cure, then the glass slide with adhered lattices was moved to an oven for 72 h at 80 °C. Then, the slide with adhered lattices was subjected to oxygen plasma (0.35 mbar, 100% O_2 gas flow, 20 min) using a Zepto plasma cleaner equipped with a W6 vacuum chamber (Diener Electronic), then submerged in a 1 wt.% solution of PEI in milli-Q water for 5 min and rinsed in 2 × 100 mL milli-Q water. A sensitizing Sn^{2+} solution was prepared by combining 1 g $SnCl_2$, 36 mL milli-Q water, and 4 mL of HCl (36.5–38%) and vortexing until the solution cleared. The glass slide with adhered lattices was fully submerged in the sensitizing solution, agitated to remove trapped bubbles, and allowed to sit for 10 min, then removed and rinsed in 2 × 100 mL milli-Q water. The Pd^{2+} activating solution was prepared by combining 20 mg $PdCl_2$, 150 mL milli-Q water, and 3 mL of 37 wt.% HCl, then sonicating and agitating for ≈1 h to fully solvate the solids. 40 mL of this solution was set aside and the substrate with adhered lattices submerged, 10 µL of the Sn^{2+} sensitizing solution was added, and the mixture was homogenized by gently swirling. Lattices were allowed to sit in the activating solution for 10 min before rinsing in 2 × 100 mL milli-Q water. The electroless Nickel plating solution (Caswell, Inc.) was prepared by combining 2 mL of part A, 6 mL of part B, and 32 mL of milli-Q water in a speed mix container and manually agitating to homogenize. It was noted that this solution is a proprietary formulation from a commercial vendor. The solution was capped and placed in a 75 °C oven for 30 min, then the activated lattices were quickly transferred into the pre-heated solution, loosely re-capped to avoid pressurization due to gas evolution, and returned to the 75 °C oven for the target duration (typically 10 or 20 min). The plating bath was then removed from the oven and the Ni-plated lattices were removed from the bath and rinsed in 2 × 100 mL milli-Q water. A gold plating bath (24K Bright Gold, Gold Plating Services) was heated in a Jewel Master Pro HD (Gold Plating Services) to 60 °C and OCV set to 3.0 V; the cathode was clipped to the tail of a nickel-plated lattice, then completely submerged in the gold plating bath to close the circuit. Woodpile lattice electrodes were plated for specified time intervals (10 or 20 min); stagger-stack lattices were plated until they reached a total mass of 20 mg.

Scanning Electron Microscopy: Lattices were systematically imaged in the XY plane and as XZ and YZ cross-sections achieved by cryo-fracturing samples in a liquid N_2 bath along selected planes. The SEM micrographs of Figures 1, 2, and 4 were collected by sputter-coating with a 10 nm layer of a Pt/Pd alloy before imaging in a field-emission scanning electron microscope (Zeiss Ultra55) at a 10 kV accelerating voltage. The EDS mapping of Figure S5 (Supporting Information) was conducted on a field-emission scanning electron microscope (Zeiss Gemini 560) fitted with an Oxford Instruments Ultim Max EDS detector at a 20 kV accelerating voltage.

Cell Fabrication and Assembly: The base of the electrochemical cell with dimensions of 50 mm × 50 mm × 12 mm was built from UV curable resin using a Phrozen Sonic Mini 8K printer. A silica microscope slide of thickness 0.5 µm was embedded into the base for direct visualization of the concentration field via fluorescence microscopy. Flow fields cast from PDMS housed the electrodes. The fluorescent half-cell consisted of a print-and-plate electrode on a 13 mm x 3 mm rectangular flow field designed to snugly fit the electrode inside. The non-fluorescent half-cell has a 2 cm x 1 cm serpentine flow field that can be used with various chemistries.

Two sets of experiments were conducted; the first was a proof-of-concept experiment to demonstrate the functionality of the print-and-plate electrodes, and the second was a 3D imaging experiment to capture the local concentration of H_2AQDS in a specific region of the electrode. For the proof-of-concept experiment, humidified hydrogen gas at ambient pressure was used with a Pt-coated gas diffusion electrode on the non-fluorescent half-cell. For the 3D imaging experiment, the non-fluorescent half-cell electrolyte was 20 mM $VOSO_4$ and 20 mM V_2O_5 in 1 M H_2SO_4 flowing through a 2 cm x 1 cm commercially available Avcarb MGL280 carbon paper electrode to provide a stable reference of 50% SOC for measurement. During assembly, the print-and-plate electrode, and the corresponding PDMS channel was wetted with 1 M H_2SO_4 to prevent air bubbles from forming inside the cell. The half-cells, separated by an ion-exchange membrane (Nafion 212 soaked in 1 M H_2SO_4), were compressed between the 3D printed base and an acrylic endplate with bolts.

Confocal Microscopy: For the proof-of-concept experiment of Figure 3, 10 mM AQDS was distributed in 1 M H_2SO_4 via a syringe pump at 5 ml h^{-1} for the duration of the experiment. Images for Figure 3 were collected on the Leica Thunder widefield microscope using a 5x objective lens with a numerical aperture of 0.12. To capture the images, a SP-150e Biologic potentiostat was used to apply a sequence of stepped voltages for 30 s and then let the cell return to OCV for 10 seconds. Voltages were 50, 100, 150, and 175 mV versus OCV, respectively. A cropped portion of the raw image series is shown in Figure 3. The 3D state of charge mapping experiment was conducted on an Andor Dragonfly confocal microscope using a 16x glycerol immersion lens. Both 20 mM vanadium-bearing and 10 mM AQDS-bearing electrolytes were pumped into the cell at 10 mL h^{-1} with a PHD ULTRA syringe pump for the fluorescent and OCV images. A 772 µm x 772 µm area centered in Y and near the inlet of the electrode was selected to capture the local concentration field in a single XY plane of the electrode. For each of three imaging conditions 1) open-circuit-voltage (OCV, 10 mM AQDS, 1 M H_2SO_4), 2) applied potential = −1.2 V (10mM AQDS, 1 M H_2SO_4), and 3) 100% SOC, a control solution composed of 10 mM H_2AQDS in 1 M H_2SO_4 representing the case of SOC = 1, a z-stack spanning 130 µm with a voxel size of 0.75 µm x 0.75 µm x 2 µm in XYZ was collected. Several voltages were tested to find the maximum voltage that could be applied without triggering hydrogen evolution. Consequently, a constant voltage of −1.2 V was applied using a SP-150e Biologic potentiostat. To establish the upper bound of fluorescence for the SOC calibration, we prepared a 100% SOC solution of H_2AQDS ex situ in a glovebox and injected it into the cell at 2 mL h^{-1} to decrease oxygen effects. The OCV, operating (applied potential = -1.2 V), and 100% SOC image stacks were each repeated 12 times consecutively and averaged to increase the signal-to-noise ratio.

Conversion of Raw Fluorescence Maps to State of Charge Maps: z-stacks at the same position were recorded under three conditions: 1) open-circuit voltage (OCV, 10 mM AQDS, 1 M H_2SO_4), 2) applied potential = −1.2 V (10 mM AQDS, 1 M H_2SO_4), and 3) a control solution composed of 10 mM H_2AQDS in 1 M H_2SO_4 representing the case of SOC = 1. Image processing was conducted in ImageJ. First, the OCV background data set 1) was subtracted from the 1.2 V data set (2) to afford stack A, which represents the background-subtracted fluorescence signal during operation. Then, background (1) was subtracted from the 100% SOC calibration set (3) to afford stack B, which represents the background-subtracted fluorescence signal for the case of SOC = 1. Then, B was masked to convert sub-threshold pixels (e.g., pixels from the interior of filaments) to NaN (not a number). The threshold cutoff was estimated visually and set to gray value 10, so that all pixels of lower gray value was set to NaN, while larger gray values were preserved, affording z-stack C. z-stack A was divided by z-stack C to afford crude SOC map D; pixels set to NaN in C were still NaN in D. z-stack D was trimmed in ImageJ by using Process > Math > Min and setting the minimum to 0, then by using Process > Math > Max and setting the maximum to 1, affording z-stack E, in which all pixel values lie between 0 and 1 or were set to NaN. This SOC map was used to estimate the mean SOC through the entire stack. Applying the "fire" lookup table in ImageJ and setting the histogram lower and upper bounds to 0 and 1, respectively, affords the color maps of Figure 5b and Movie S7 (Supporting Information).

Numerical Simulations: The numerical simulation of the governing partial differential equations (PDEs) treated the incompressible flow problem separately from the reaction simulation. The geometry was defined as a collection of cylindrical rods that were allowed to overlap with each other. A coarse spatial grid was constructed with a 5.0 µm box size and extended with two levels of mesh refinement. Each mesh refinement doubles the spatial resolution on boxes containing a solid / liquid boundary plus a buffer of one adjacent cell. The fully refined spatial grid resolved the boundary to a 1.25 µm resolution and contained 780–840 million cells for the lattice designs considered. The PDE for the fluid flow was taken to be the incompressible Navier-Stokes equation with constant density and viscosity. The boundary conditions for flow were no slip at the four walls

exceptingexcept the inlet and outlet, which were assigned fixed pressures. The numerical simulation was performed with an MPI C++ code derived from the incflo library.[43] The flow was first simulated to a steady state at the coarse level, with time steps terminating after a convergence criterion was achieved. The results of this were then upsampled to a grid with one level of mesh refinement and again simulated to a steady state. This procedure was repeated once more to simulate the final grid. The upsampling procedure significantly reduced the time required to simulate the fluid flow. Each geometry was simulated multiple times to find a pressure nearly consistent with the experimental condition of a 10.0 mL h^{-1} volumetric pumping rate. The staggered, stacked, and stagger-stack lattices respectively required pressures of 244, 419 and 136 Pa.

The electrochemical reaction was modeled with the Nernst-Planck equation including terms for advection, diffusion, and electrochemical reactions with Butler-Volmer kinetics. The phenomenon of electromigration was ignored in this simulation because it was negligible compared to advection and diffusion. The justification for this was that a strong supporting electrolyte of 1 M H_2SO_4 minimizes electric fields in the liquid phase. Complete simulations including electromigration on simpler reaction conditions demonstrated that including this term had a negligible effect on the results but it made the program significantly slower. For each reaction simulation, the corresponding incompressible fluid flow was taken as a given that does not change during the reaction. The boundary condition at the inlet was a flow of 20 mM AQDS at a nearly oxidized state of charge (approaching zero) because the incoming solution is equilibrated with air. The simulation was originally run at this higher AQDS concentration of 20 mM, and the results, which were linear in the total concentration, were subsequently adjusted to reflect a 10 mM total AQDS concentration after an earlier experimental protocol was revised. The boundary conditions for the solid / liquid interface were a constant applied voltage. The applied voltage was described against a hypothetical reference electrode of AQDS / H_2AQDS at 0.5 SOC, so zero volts on this scale implies that at equilibrium the local SOC around the wire would be 0.5. The numerical simulation was performed with an MPI C++ code derived from previously published work.[28] Reaction time steps were carried out until a criterion for small changes in concentration was reached. The same upsampling technique was used to accelerate convergence as in the flow simulation, with the entire electrode first simulated to a steady state on the 5.0 µm grid before it was simulated on the refined grids. Reaction simulations were carried out at multiple voltages. Because the voltage offset to OCV was difficult to simulate, the voltage was set iteratively to match the experimentally determined utilization fraction, rounding the applied voltage to the nearest one millivolt.

Supporting Information

Supporting Information is available from the Wiley Online Library or from the author.

Acknowledgements

The authors gratefully acknowledge support from the Department of Energy through the Office of Basic Energy Sciences (DE-SC0020170). M.D.N., a post-baccalaureate researcher, was supported in part by NSF DMR-2011754 (Harvard MRSEC), NSF DMR-2122195 (NTU PREM), the Harvard John A. Paulson School of Engineering and Applied Sciences post-baccalaureate program, and the Harvard Research Scholar Initiative. The authors thank Taobo Wang for preparing 100% SOC solutions for fluorescence calibrations. The Andor Dragonfly confocal and Leica Thunder widefield microscopes were provided by Harvard MRSEC (DMR-2011754). S.E.M. data were collected at the electron microscopy facilities at the Harvard University Center for Nanoscale Systems (CNS), a member of the National Nanotechnology Coordinated Infrastructure Network (NNCI), which is supported by the National Science Foundation under NSF award no. ECCS-2025158. The authors thank Timothy Cavanaugh for EDS mapping of a cryo-fractured sample.

Conflict of Interest

The authors declare no conflict of interest.

Data Availability Statement

The data that support the findings of this study are openly available in [Zenodo] at [https://doi.org/10.5281/zenodo.12802868], reference number [12802868].

Keywords

3D-printing, direct ink writing, electrochemistry, flow batteries, flow cells, porous electrodes

Received: October 17, 2024
Revised: February 18, 2025
Published online:

[1] J. Noack, N. Roznyatovskaya, T. Herr, P. Fischer, *Angew. Chemie – Int. Ed.* **2015**, *54*, 9776.
[2] S. A. Mousavi Shaegh, N. T. Nguyen, S. H. Chan, *Int. J. Hydrogen Energy.* **2011**, *36*, 5675.
[3] G. F. Swiegers, A. L. Hoang, A. Hodges, G. Tsekouras, C. Y. Lee, K. Wagner, G. Wallace, *Curr. Opin. Electrochem.* **2022**, *32*, 100881.
[4] S. C. Perry, C. Ponce de León, F. C. Walsh, *J. Electrochem. Soc.* **2020**, *167*, 155525.
[5] L. F. Arenas, C. Ponce de León, F. C. Walsh, *J. Electrochem. Soc.* **2020**, *167*, 023504.
[6] A. Molaei, F. Ahmed, U. Ail, X. Crispin, *Chem. Pap.* **2023**, *77*, 1941.
[7] M. A. Alkhadra, X. Su, M. E. Suss, H. Tian, E. N. Guyes, A. N. Shocron, K. M. Conforti, J. P. De Souza, N. Kim, M. Tedesco, K. Khoiruddin, I. G. Wenten, J. G. Santiago, T. A. Hatton, M. Z. Bazant, *Chem. Rev.* **2022**, *122*, 13547.
[8] A. Bhattarai, N. Wai, R. Schweiss, A. Whitehead, T. M. Lim, H. H. Hng, *J. Power Sources.* **2017**, *341*, 83.
[9] W. Chen, J. Kang, Q. Shu, Y. Zhang, *Energy.* **2019**, *180*, 341.
[10] J. Kim, H. Park, *J. Power Sources.* **2022**, *545*, 231904.
[11] S. J. Yoon, S. Kim, D. K. Kim, *Energy.* **2019**, *172*, 26.
[12] Y. Zhang, X. Zhang, Z. Xu, D. Zhang, W. Yu, Y. Zhang, L. Liu, J. Liu, C. Yan, *J. Power Sources.* **2022**, *552*, 232241.
[13] R. Schweiss, C. Meiser, F. W. T. Goh, *Chem. Electro. Chem.* **2017**, *4*, 1969.
[14] R. Banerjee, N. Bevilacqua, A. Mohseninia, B. Wiedemann, F. Wilhelm, J. Scholta, R. Zeis, *J. Energy Storage.* **2019**, *26*, 100997.
[15] B. Sun, M. Skyllas-Kazacos, *Electrochim. Acta.* **1992**, *37*, 1253.
[16] B. Sun, M. Skyllas-Kazacos, *Electrochim. Acta.* **1992**, *37*, 2459.
[17] B. A. Simon, A. Gayon-Lombardo, C. A. Pino-Muñoz, C. E. Wood, K. M. Tenny, K. V. Greco, S. J. Cooper, A. Forner-Cuenca, F. R. Brushett, A. R. Kucernak, N. P. Brandon, *Appl. Energy.* **2022**, *306*, 117678.
[18] A. A. Wong, M. J. Aziz, *J. Electrochem. Soc.* **2020**, *167*, 110542.
[19] J. D. Milshtein, K. M. Tenny, J. L. Barton, J. Drake, R. M. Darling, F. R. Brushett, *J. Electrochem. Soc.* **2017**, *164*, E3265.
[20] M. R. Gerhardt, A. A. Wong, M. J. Aziz, *J. Electrochem. Soc.* **2018**, *165*, A2625.
[21] J. L. Barton, J. D. Milshtein, J. J. Hinricher, F. R. Brushett, *J. Power Sources.* **2018**, *399*, 133.
[22] J. Houser, A. Pezeshki, J. T. Clement, D. Aaron, M. M. Mench, *J. Power Sources.* **2017**, *351*, 96.
[23] C. S. Cho, J. K. Chen, C. C. Li, *Chem. Mater.* **2022**, *34*, 8127.
[24] K. M. Tenny, A. F. Cuenca, Y. M. Chiang, F. R. Brushett, *J. Electrochem. Energy Convers. Storage.* **2020**, *17*, 041010.

[25] K. M. Tenny, V. S. Lakhanpal, R. P. Dowd, V. Yarlagadda, T. Van Nguyen, *J. Electrochem. Soc.* **2017**, *164*, A2534.
[26] X. L. Zhou, T. S. Zhao, Y. K. Zeng, L. An, L. Wei, *J. Power Sources.* **2016**, *329*, 247.
[27] K. Sun, T. S. Wei, B. Y. Ahn, J. Y. Seo, S. J. Dillon, J. A. Lewis, *Adv. Mater.* **2013**, *25*, 4539.
[28] S. Dussi, C. H. Rycroft, *Phys. Fluids.* **2022**, *34*.
[29] B. Y. Ahn, E. B. Duoss, M. J. Motala, X. Guo, S. Il Park, Y. Xiong, J. Yoon, R. G. Nuzzo, J. A. Rogers, J. A. Lewis, *Science.* **2009**, *323*, 1590.
[30] M. van der Heijden, M. Kroese, Z. Borneman, A. Forner-Cuenca, *Adv. Mater. Technol.* **2023**, *8*, 2300611.
[31] V. A. Beck, A. N. Ivanovskaya, S. Chandrasekaran, J. B. Forien, S. E. Baker, E. B. Duoss, M. A. Worsley, *Proc. Natl. Acad. Sci. USA.* **2021**, *118*, 1.
[32] I. Ohno, *Mater. Sci. Eng. A.* **1991**, *146*, 33.
[33] M. Charbonnier, M. Alami, M. Romand, *J. Electrochem. Soc.* **1996**, *143*, 472.
[34] J. Zhou, H. Zhang, R. Wang, Z. Li, H. Li, P. Duan, S. Shang, Y. Zhang, Z. Wang, W. Ge, H. Lan, X. Zhu, *Virtual Phys. Prototyp.* **2023**, *18*, 2268602.
[35] C. W. Ha, P. Prabhakaran, Y. Son, *3D Print. Addit. Manuf.* **2019**, *6*, 165.
[36] M. Abdulrhman, A. Zhakeyev, C. M. Fernández-Posada, F. P. W. Melchels, J. Marques-Hueso, *Flex. Print. Electron.* **2022**, *7*, 025006.
[37] A. A. Wong, S. M. Rubinstein, M. J. Aziz, *Cell Reports Phys. Sci.* **2021**, *2*, 100388.
[38] J. O. Hardin, T. J. Ober, A. D. Valentine, J. A. Lewis, *Adv. Mater.* **2015**, *27*, 3279.
[39] J. C. Conrad, J. A. Lewis, *Langmuir.* **2008**, *24*, 7628.
[40] B. Huskinson, M. P. Marshak, C. Suh, S. Er, M. R. Gerhardt, C. J. Galvin, X. Chen, A. Aspuru-Guzik, R. G. Gordon, M. J. Aziz, *Nature.* **2014**, *505*, 195.
[41] M. R. Gerhardt, L. Tong, R. Gómez-Bombarelli, Q. Chen, M. P. Marshak, C. J. Galvin, A. Aspuru-Guzik, R. G. Gordon, M. J. Aziz, *Adv. Energy Mater.* **2017**, *7*, 1601488.
[42] A. M. Graf, T. Cochard, K. Amini, M. S. Emanuel, S. M. Rubinstein, M. J. Aziz, *Energy Adv.* **2024**, *3*, 2468.
[43] K. Sverdrup, A. Almgren, N. Nikiforakis, *Phys. Fluids.* **2019**, *31*, 093102
[44] W. Zhang, A. Almgren, V. Beckner, J. Bell, J. Blaschke, C. Chan, M. Day, B. Friesen, K. Gott, D. Graves, M. Katz, A. Myers, T. Nguyen, A. Nonaka, M. Rosso, S. Williams, M. Zingale, *J. Open Source Softw.* **2019**, *4*, 1370.